

Published in final edited form as:

ACS Nano. 2012 June 26; 6(6): 4694–4701. doi:10.1021/nn204352r.

Family of Enhanced Photoacoustic Imaging Agents for High Sensitivity and Multiplexing Studies in Living Mice

Adam de Zerda^{1,2}, Sunil Bodapati¹, Robert Teed¹, Salomon Y. May¹, Scott M. Tabakman³, Zhuang Liu^{3,4}, Butrus T. Khuri-Yakub², Xiaoyuan Chen^{1,5}, Hongjie Dai³, and Sanjiv S. Gambhir^{1,6}

¹Molecular Imaging Program at Stanford, Department of Radiology and Bio-X Program, Stanford University, Palo Alto, CA 94305, USA

²Department of Electrical Engineering, Stanford University, Palo Alto, CA 94305, USA

³Department of Chemistry, Stanford University, Palo Alto, CA 94305, USA

⁴Institute of Functional Nano & Soft Materials (FUNSOM), Soochow University, Suzhou, Jiangsu, 215123, China

⁵Laboratory of Molecular Imaging and Nanomedicine, National Institute of Biomedical Imaging and Bioengineering (NIBIB), National Institutes of Health (NIH), Bethesda, MD 20892, USA

⁶Department of Bioengineering, Department of Materials Science & Engineering, Stanford University, Palo Alto, CA 94305, USA

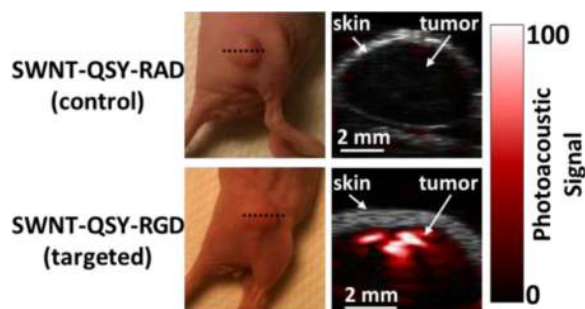
Abstract

Photoacoustic imaging is a unique modality that overcomes to a great extent the resolution and depth limitations of optical imaging while maintaining relatively high-contrast. However, since many diseases will not manifest an endogenous photoacoustic contrast, it is essential to develop exogenous photoacoustic contrast agents that can target diseased tissue(s). Here we present a family of novel photoacoustic contrast agents that are based on the binding of small optical dyes to single walled carbon nanotubes (SWNT-dye). We synthesized five different SWNT-dye contrast agents using different optical dyes, creating five “flavors” of SWNT-dye nanoparticles. In particular, SWNT that were coated with either QSY₂₁ (SWNT-QSY) or Indocyanine Green (SWNT-ICG) exhibited over 100-times higher photoacoustic contrast in living animals compared to plain SWNTs, leading to subnanomolar sensitivities. We then conjugated the SWNT-dye conjugates with cyclic Arg-Gly-Asp (RGD) peptides to molecularly target the $\alpha_v\beta_3$ integrin, which is associated with tumor angiogenesis. Intravenous administration of these tumor-targeted imaging agents to tumor-bearing mice showed significantly higher photoacoustic signal in the tumor than in mice injected with the untargeted contrast agent. Finally, we were able to spectrally separate the photoacoustic signals of SWNT-QSY and SWNT-ICG in living animals injected subcutaneously with both particles in the same location, opening the possibility for multiplexing *in vivo* studies.

*sgambhir@stanford.edu.

Conflict of Interest: The authors declare no competing financial interest.

Supporting Information Available: *In vitro* characterization of the particles including optical stability upon peptide conjugation, serum-stability, photobleaching and cell-uptake study. This material is available free of charge *via* the Internet at <http://pubs.acs.org>.



Keywords

carbon nanotubes; SWNT; molecular imaging; photoacoustic imaging; multiplexing

Visualizing abnormalities in a living subject has traditionally been done through various medical imaging modalities such as X-ray computed tomography (CT), magnetic resonance imaging (MRI) and ultrasound. In the past decades many new medical imaging modalities that are based on visible and near infra-red wavelengths have emerged such as optical coherence tomography, whole-body fluorescence imaging and others. However, due to the relatively high optical scattering of living tissue, most of the optical imaging modalities are limited in their ability to visualize objects deeper than a few millimeters in the body with reasonable resolution and signal-to-noise ratio.

Photoacoustic imaging is an emerging modality that brings significant promise to enhance the depth of penetration as well as spatial resolution, while maintaining the high contrast of optical imaging.¹ Contrary to traditional optical imaging where light must travel in and out of the tissue, with photoacoustic imaging, light only travels into the tissue, where it is being converted by optical absorbers to pressure waves through the photoacoustic effect.²

The primary use of photoacoustic imaging has traditionally been visualizing endogenous absorbers in the body such as hemoglobin. This allowed the visualization of the blood vessels network in three dimensions in various living tissues.^{3–5} Moreover, by acquiring a partial photoacoustic spectrum, the blood oxygen saturation levels can be measured, allowing the visualization of hypoxemia.⁶ In addition, the endogenous absorbing molecule melanin has been imaged using photoacoustic imaging in various scenarios, including melanoma – a skin cancer with typically elevated melanin levels.⁷

In order to allow the visualization of other biomarkers besides hemoglobin and melanin by photoacoustic imaging, exogenous contrast agents must be used.⁸ These contrast agents should exhibit high optical absorption characteristics in order to produce a high photoacoustic signal, and may or may not be molecularly targeted to a specific biomarker in the tissue. Significant work on photoacoustic contrast agents has been focused on gold nanoparticles^{9–14} as well as other kinds of nanoparticles^{15–17} and small molecules.¹⁸ However, most of these contrast agents suffer from poor delivery, leading to only small amounts of the injected dose to accumulate in the target tissue. This problem is further amplified in molecularly targeted contrast agents. We recently reported on single walled carbon nanotubes (SWNTs) that are coated by Indocyanine Green (ICG).¹⁹ The resulting nanoparticle exhibited high optical absorbance while maintaining the high tumor-targeting abilities previously reported of plain SWNTs.⁸

In this work, we report on a general method to prepare a dye-enhanced SWNTs photoacoustic imaging agents by coating any one of five different small molecule dyes onto

the surface of a SWNT. We show that the resulting imaging agents can target cancer-specific receptors in tumor-bearing mice, exhibit unprecedented high sensitivity and can be imaged simultaneously (multiplexed). The ability to multiplex several imaging agents based on their different photoacoustic spectrum^{20, 21} is highly desirable as it may allow in the future visualizing multiple molecular processes in a living tissue simultaneously.

Results

We have recently reported on the conjugation of cyclic Arg-Gly-Asp (RGD) peptides to pegylated SWNTs²² (SWNT-RGD). We then reported on their use as photoacoustic imaging agents to visualize $\alpha_v\beta_3$ integrin⁸, which is over-expressed in tumor neovasculature. We then also reported on the binding of Indocyanine Green (ICG) to the surface of the SWNTs through pi-pi stacking.¹⁹ This loading of ICG onto the surface of the SWNTs has resulted in significantly better *in vivo* sensitivity than plain SWNTs. In this work we generalize the method and show it works for a number of optical dyes and quenchers including QSY₂₁, Methylene Blue (MB), Cyanine dyes such as Cy5.5, and Melanin (Fig. 1a). Control untargeted SWNT-dye particles were conjugated to a mutated non-targeted peptide, RAD that does not bind to $\alpha_v\beta_3$ integrin (see **Methods** for more details on syntheses).

The ultra-high surface area to volume ratio of the SWNTs allowed for efficient loading of the optical dyes onto the nanotubes surface. The SWNT-dye conjugates exhibited a significant increase in the optical absorption compared to plain SWNTs of 120%, 88% and 30% for Methylene Blue, Cy5.5 and Melanin, respectively (Fig. 1b). Of highest interest were ICG and QSY₂₁ dyes whose conjugates with SWNTs led to 20 and 17-fold increase in the particles' optical absorption, respectively (Fig. 1c). Furthermore, the spectra of SWNT-QSY and SWNT-ICG peak at different wavelengths; 710 nm and 780 nm, respectively. We therefore selected SWNT-QSY and SWNT-ICG as the candidate molecular imaging agents to demonstrate multiplexing in this work. Importantly, the nanoparticles conjugated with RAD and RGD had nearly identical absorption spectra (see Supporting Information and Supplementary Fig. S1), suggesting that the peptide conjugation did not interfere with the particle's photoacoustic signal.

We constructed a non-absorbing and non-scattering agarose phantom with inclusions of SWNT-QSY-RGD and SWNT-ICG-RGD at increasing concentrations from 0.5 nM to 121.5 nM in multiples of 3 (n = 3 inclusions per concentration). We used our custom-made photoacoustic imaging system (see **Methods** and Supplementary Fig. S5) and scanned the phantom at 710 nm and 780 nm for the QSY- and ICG-coated particles, respectively. The photoacoustic signal produced by the SWNT-QSY-RGD and SWNT-ICG-RGD particles highly correlated with the nanoparticle concentration ($R^2 = 0.99$ and 0.98 respectively) (Fig. 1d).

We further validated that the new particles are stable in serum (see Supplementary Information and Supplementary Fig. S2). The particle's photobleaching (*i.e.* loss of optical absorption due to continuous light exposure to the particle) was characterized and found to be relatively small. The optical absorption of SWNT-ICG was reduced by only 30% after 60 min of laser irradiation at normal power density of 8 mJ/cm². SWNT-QSY, however, showed higher light-sensitivity, resulting in a 50% reduction in optical absorption after 7 min of laser irradiation of the same intensity (see Supplementary Information and Supplementary Fig. S3). Finally, cell uptake studies showed specific binding of SWNT-QSY-RGD and SWNT-ICG-RGD to U87MG cells, compared with control particles SWNT-QSY-RAD and SWNT-ICG-RAD, respectively (see Supplementary Information and Supplementary Fig. S4).

We then tested the particle's sensitivity in living subjects by subcutaneously injecting the lower back of mice ($n = 3$) with 30 μl of SWNT-QSY-RGD mixed with matrigel at increasing concentrations between 500 pM to 122 nM. Matrigel alone produced no significant photoacoustic signal (data not shown). All animal experiments were performed in compliance with the Guidelines for the Care and Use of Research Animals established by the Stanford University Animal Studies Committee. Upon injection, the matrigel solidified, fixing the nanoparticles in place and three-dimensional (3D) ultrasound and photoacoustic images of the inclusions were acquired (Fig. 2a). While the ultrasound image visualized the mouse anatomy (*e.g.*, skin and inclusion edges), the photoacoustic image revealed the nanoparticles' contrast in the mouse tissue. The photoacoustic signal from each inclusion was quantified using a three dimensional region of interest (ROI) drawn over the inclusion volume. We observed a linear correlation ($R^2 = 0.97$) between the nanoparticles concentration and the corresponding photoacoustic signal (Fig. 2b), as was previously observed with SWNT-ICG-RGD¹⁹. Tissue background signal was calculated as the average photoacoustic signal in areas where no nanoparticles were injected. Extrapolation of the signal-concentration graph reveals that 450 pM of SWNT-QSY-RGD produce the equivalent photoacoustic signal as the tissue background (*i.e.*, signal to background ratio = 1). This value represents over 100-times improvement in sensitivity compared to plain SWNTs and is comparable to the 170 pM sensitivity limit that has been previously calculated for SWNT-ICG-RGD.

We then tested the nanoparticles targeting ability in living mice. Mice bearing U87MG tumor xenografts (150 mm³ in size) were injected through the tail vein (IV) with 200 μl of either SWNT-QSY-RGD (targeted) or SWNT-QSY-RAD (untargeted control) or the SWNT-ICG conjugates ($n = 3$ mice per group) at a concentration of 1.2 μM . Importantly, no acute cytotoxicity or distress were observed in the animals upon injection and up to a period of one week post-injection. We acquired 3D photoacoustic and ultrasound images of the entire tumor area before and 2 h after the injection. Mice injected with the RGD-targeted nanoparticles showed significantly higher photoacoustic signal in the tumor compared with the control group injected with the RAD control particles (Fig. 3a). The ultrasound images were used for visualizing the boundaries of the tumor as well as to validate that no significant movement (beyond 100 μm) had occurred throughout the experiment. Before the injection, the photoacoustic signal in the tumor is due to the tumor's blood vessels, while after the injection, the photoacoustic signal is due to both the blood vessels and the nanoparticles. To remove out the background blood signal, subtraction images were calculated as the post-injection minus the pre-injection images, leaving the image primarily with the contrast made by the nanoparticles (Fig. 3a). Measurement of the photoacoustic signal from a 3D ROI around the tumor (Fig. 3b) showed that the photoacoustic signal in the tumor was significantly higher in mice injected with the RGD-targeted nanoparticles as compared with the control particles ($p < 0.01$). At 2 h post-injection, mice injected with SWNT-QSY-RGD showed over 3-times higher photoacoustic signal increase in the tumor than mice injected with the control SWNT-QSY-RAD.

While the optical absorption spectra of SWNT-QSY and SWNT-ICG overlap, they are not identical, which may allow to spectrally unmix their signals, even at situations where they are spatially co-localized. We prepared an optically clear agarose-based phantom with five wells in which SWNT-QSY and SWNT-ICG were mixed in respective concentrations of 0:100, 25:75, 50:50, 75:25, 100:0 (in units of nM). Photoacoustic images of the phantom at 700, 730, 760, 780, 800 nm were taken (Fig. 4a) and used in a least squares method (see **Methods** for more details) to unmix the photoacoustic signals produced by the SWNT-QSY and the SWNT-ICG particles. No cross-signaling between the SWNT-QSY and SWNT-ICG channels was observed in the wells with either pure SWNT-QSY or pure SWNT-ICG. In

wells with both SWNT-QSY and SWNT-ICG, appropriate proportion of signal of both particles was observed (Fig. 4b).

Finally, we injected 30 μ l of an equal mixture of SWNT-QSY and SWNT-ICG at 50 nM subcutaneously to a living mouse flank (Fig. 5a). Control injections of 30 μ l of SWNT-QSY and SWNT-ICG alone were injected subcutaneously to the mouse flank as well. Photoacoustic images at 700, 730, 760, 780, 800 nm were used to spectrally unmix the SWNT-QSY and the SWNT-ICG signals. The SWNT-QSY injection site showed only SWNT-QSY signal (Fig. 5b) and the SWNT-ICG injection site showed primarily SWNT-ICG signal (Fig. 5c). Importantly, the site that was injected with the equal mixture of particles showed both SWNT-QSY and SWNT-ICG signal (Fig. 5d). At the area of injection, a slight separation of photoacoustic signals of the two channels (SWNT-QSY and SWNT-ICG) was observed. These image reconstruction artifacts are likely caused by slight movements of the mouse between the acquisition of consecutive photoacoustic images at different wavelengths, as well as differences in light tissue distribution across the five wavelengths.

Discussion

We have synthesized, characterized and demonstrated the application of multiple dye-enhanced SWNTs as ultra-high sensitivity photoacoustic imaging agents. For SWNT-QSY and SWNT-ICG, concentrations as low as 450 pM and 170 pM were estimated to be the *in vivo* sensitivity limits, respectively, representing over 100-times improvement over plain SWNTs.⁸ This improvement is likely due to both the higher optical absorption of the particles as well as the fact that the new particle's absorption peak is further red-shifted than plain SWNTs, where the background tissue photoacoustic signal is greatly reduced. Most importantly, intravenous injection of RGD-targeted SWNT-QSY and SWNT-ICG particles to tumor-bearing mice led to significantly greater accumulation of the particles in the tumors compared to non-targeted control particles. The fact that plain SWNT-RGD target tumors in living mice does not necessarily imply that SWNT-dye-RGD would also target tumors in living mice. This is because the additional dye-coating may increase the size and molecular weight of the particles and change their surface charge and zeta-potential. Finally, we demonstrated the ability to multiplex the signals from SWNT-QSY and SWNT-ICG both *in vitro* as well as in living mice. This entails not only reater sensitivity for earlier detection of diseases, but also greater specificity by providing molecular information on two molecular processes simultaneously.

While small-molecule optical dyes have lower optical absorption, they are also significantly smaller than nanoparticles. For example, the ratio between the absorption coefficient of ICG and its molecular weight is still 7-times greater than that of a plain SWNT. This suggests that creating a carrier for small optical dyes, such as SWNT, may be highly beneficial, as indeed shown in this work. Determining the exact number of dye molecules per SWNT is challenging due to synergistic or quenching effects the dyes may be exhibiting on themselves or the SWNT. However, assuming such effects are not taking place in this SWNT-dye system, the enhancement in optical absorption of the SWNT-dye conjugates would represent the number of dye molecules times the dye absorption coefficient. Hence, the number of dyes per SWNT can be estimated to be: 33, 130, 710, and 2032 for Cy5.5, Methylene Blue, ICG and QSY²¹, respectively. It is likely that the difference among the dyes is a result of their ability to form pi-pi stacking interactions with the SWNT surface.

Photoacoustic imaging has been primarily used to visualize endogenous absorbers such as hemoglobin and melanin.^{3-5, 7} However, in order to visualize molecular characteristics of a tumor, an exogenous contrast agent that is specific for a given molecular target is required²³.

However, the main challenge in designing a photoacoustic imaging agent is that sufficient amounts of the agent need to reach the target site and create a detectable and specific signal. Most nanoparticles reported to date to produce strong photoacoustic signal suffer from significant and rapid uptake by the reticuloendothelial system (RES), likely preventing the particles from accumulating at the tumor site in sufficient amounts. The SWNTs used here are 1–2 nm in diameter and 50–300 nm in length. We believe that this size is maintained even after the conjugation of the small optical dyes to the SWNT surface, as the dyes are conjugated directly to the surface of the nanotube, under the polyethylene-glycol (PEG). This likely allows the particles to maintain the favorable bio-distribution of plain SWNT-RGD.²² Hence, the dye-enhanced SWNTs presented in this work offer both unprecedented photoacoustic sensitivity as well as good tumors targeting capabilities upon intravenous injection. We have also previously published pilot toxicology studies of the SWNTs with encouraging results in mouse models²⁴ and observed the SWNTs are able to be excreted *via* the biliary pathway.^{25, 26}

Conclusion

The dye-enhanced SWNT photoacoustic imaging agents reported here have the capability to bind to molecular targets in living animals while maintaining a very high photoacoustic signal and allowing multiplexing studies. No other imaging modality or imaging agent can achieve both sub-nM sensitivity at high depths of penetration and sub-millimeter spatial resolution as can be achieved with photoacoustic imaging of dye-enhanced SWNTs. To our knowledge, this is the first demonstration of multiplexing photoacoustic imaging agents that are capable to molecularly target tumors in living animals.

Methods

Dye-enhanced SWNTs Synthesis

A complete description of the synthesis of SWNT-RGD and SWNT-RAD can be found elsewhere.²² PEGylated SWNTs at a concentration of 250 nM were incubated overnight in water with 1mM Indocyanine Green (ICG), QSY₂₁ or Cy5.5, or excess of melanin or Methylene Blue. ICG (Spectrum Laboratory Products, CA) (20 mM) was dissolved in DMSO first and then added to SWNT water solutions with a final DMSO concentration of < 10% by volume. Prior to incubation with SWNTs, Cy5.5 and QSY₂₁, purchased as N-hydroxysuccinimide esters, were dissolved in DMSO and hydrolyzed overnight by dilution into deionized water. Unbound dye molecules were removed from the solution by filtration through 100 kDa centrifuge filters (Millipore) and washed 6–8 times. The SWNTs used in this work were 50–300 nm in length and 1–2 nm in diameter. The molar concentrations are based on an average molecular weight of 170 kDa per SWNT (150 nm in length and 1.2 nm in diameter).

For preparation of SWNT-R(G/A)D-ICG and SWNT-R(G/A)D-QSY, SWNTs were dispersed by sonication as described previously²² in 1,2-distearoyl-sn-glycero-3-phosphoethanolamine-PEG₅₀₀₀-NH₂ (DSPE-PEG-NH₂, NOF Corp.). Following removal of free surfactant by repeated ultracentrifuge filtration, the SWNT suspension at ~250 nM was incubated with 1 mM of ICG or 1 mM of QSY₂₁, dissolved and hydrolyzed as above), followed by ultracentrifuge filtration to remove any free dye molecules. Next, the dye-loaded SWNTs suspended by DSPE-PEG-NH₂ at ~500 nM were mixed with 0.5 mM sulfo-SMCC (Pierce) in phosphate buffered saline (PBS) and allowed to react for 2 h at room temperature. Free sulfo-SMCC was removed by repeated ultracentrifuge filtration and the resulting maleimide-activated SWNT-dye conjugate suspensions were each split into two equal aliquots. Cyclic(RGDfC) (RGD) or cyclic(RADfC) (RAD) were mixed with 20 mM tris-(2-carboxyethyl)phosphine-HCl (TCEP) in PBS adjusted to pH 8 for 15 min at room

temperature. The RGD or RAD containing TCEP was added into each aliquot of maleimide-activated SWNT-dye conjugates at a final peptide concentration of 150 μ M, and coupling was allowed to proceed for 24 h at 4 °C, followed by a final round of repeated ultracentrifugal filtration to remove free peptide.

Photoacoustic Instrumentation

Our custom-made photoacoustic system²⁷ is illustrated in Supplementary Figure 5. A tunable pulsed laser with a repetition rate of 10 Hz and a pulse width of 5 ns (Nd:YAG Surelight-III-10 connected to Surelite OPO Plus, Continuum) illuminated the object through a fiber optic ring light (50–1353 Ringlight, Fiberoptic Systems Inc.). The average energy density of the laser at the wavelengths used in this study (*i.e.*, 700, 710, 730, 760, 780 and 800 nm) was set to be ~ 8 mJ/cm² at the target site, which is below the ANSI limitation for laser skin exposure.²⁸ A 5 MHz focused transducer (25.5 mm focal length, 4 MHz bandwidth, F number of 2.0, depth of focus of 6.5 mm, lateral resolution of 600 μ m, and axial resolution of 380 μ m. A309S-SU-F-24.5-MM-PTF, Panametrics) was used to acquire both pulse-echo and photoacoustic images. In addition, high resolution ultrasound images were acquired using a 25 MHz focused transducer (27 mm focal length, 12 MHz bandwidth, F number of 4.2, depth of focus of 7.5 mm, lateral resolution of 250 μ m, and axial resolution of 124 μ m. V324-SU-25.5-MM, Panametrics). A precision xyz-stage (U500, Aerotech Inc.) with minimum step size of 1 μ m was used to move the transducer and the fiber ring along a planar 2D trajectory. At every position, the acquired signal was averaged over 4 laser pulses. The time of arrival and the intensity of the laser pulses were recorded using a silicon photodiode (DET10A, Thorlabs). This information was used to synchronize the acquisition and compensate for pulse-to-pulse variations in laser intensity. The analog photoacoustic signals were amplified using a variable gain preamplifier (5072PR/115VAC, Panametrics) and digitized using an oscilloscope (Infiniium 54825A, Agilent). The photoacoustic and ultrasound images were reconstructed as follows: the A-scan from each position of the transducer was band-pass filtered with 200% fractional bandwidth, compensated for laser intensity variation and envelope detected. The A-scans were then combined to reconstruct a 3D intensity image of the target. No further post-processing was done on the images. The ultrasound images acquired using the 5 MHz and 25 MHz transducers were aligned together using small vertical translations so that the object's skin level matches in both images. Then, photoacoustic and the high frequency ultrasound images were analyzed, co-registered and displayed using AMIDE²⁹ software.

Spectral Unmixing of the Photoacoustic Signals

In both the *in vitro* and *in vivo* experiments that showed the multiplexing capability of SWNT-QSY and SWNT-ICG, the same acquisition technique and image reconstruction algorithms were used. Initially, an ultrasound image of the object was acquired to determine the areas of interest. Then, consecutive photoacoustic images of the object at wavelengths of 700, 730, 760, 780 and 800 nm were acquired. The principal components of the photoacoustic signals of SWNT-QSY and SWNT-ICG were determined based on region of interest analysis over regions that were previously known to contain SWNT-QSY only or SWNT-ICG only. Then, least squares technique was used to create two individual images on a pixel-by-pixel basis, one for each SWNT-dye particle. Visualization of the two images was done using Amide²⁹ software, where red color was assigned to the SWNT-QSY signal and green color was assigned to the SWNT-ICG signal.

Mouse Arrangement in the Photoacoustic System

All animal experiments were performed in compliance with the Guidelines for the Care and Use of Research Animals established by the Stanford University Animal Studies Committee. Female nude mice were used for all the photoacoustic studies. The mice that were scanned

in the photoacoustic system were fully anesthetized using isoflurane delivered through a nose-cone (2% isoflurane in 100% oxygen, 2 liters per min gas flow rate). Prior to the photoacoustic scan, the areas of interest were covered with agar gel to stabilize the area and minimize any breathing and other motion artifacts. A saran wrap water bath was placed on top of the agar gel. An ultrasonic transducer, placed in the water bath, was therefore acoustically coupled to the mouse tissues. This setup allowed the ultrasonic transducer to move freely in 3D while not applying any physical pressure on the mouse.

Statistical Methods

For the tumor targeting experiment, we used the two-sided student's t-test to test the hypothesis that the group of mice injected with the RGD-targeted particles exhibited higher photoacoustic signal than mice injected with the control RAD-targeted particles.

Supplementary Material

Refer to Web version on PubMed Central for supplementary material.

Acknowledgments

We would like to acknowledge funding from the National Institute of Health (NIH) grants NCI CCNE U54 CA119367 (SSG), NCI ICMIC P50 CA114747 (SSG), and the Canary Foundation for supporting this work. A. de la Zerda acknowledges funding from the Bio-X Graduate Student Fellowship, the Department of Defense – Breast Cancer Research Program – Pre-doctoral Traineeship Award (W81XWH-09-1-0025), and the Damon Runyon Cancer Research Foundation (DRG-2094-11). The authors would also like to thank Srikant Vaithilingam, Omer Oralkan and Te-Jen Ma for helpful discussions.

References

1. Wang LV. Multiscale Photoacoustic Microscopy and Computed Tomography. *Nat Photon.* 2009; 3:503–509.
2. Bell A. On the Production and Reproduction of Sound by Light. *American Journal of Science.* 1880
3. Zhang HF, Maslov K, Stoica G, Wang LV. Functional Photoacoustic Microscopy for High-Resolution and Noninvasive in Vivo Imaging. *Nat Biotechnol.* 2006; 24:848–851. [PubMed: 16823374]
4. Laufer J, Zhang E, Raivich G, Beard P. Three-Dimensional Noninvasive Imaging of the Vasculature in the Mouse Brain Using a High Resolution Photoacoustic Scanner. *Appl Opt.* 2009; 48:D299–D306. [PubMed: 19340121]
5. de la Zerda A, Paulus YM, Teed R, Bodapati S, Dollberg Y, Khuri-Yakub BT, Blumenkranz MS, Moshfeghi DM, Gambhir SS. Photoacoustic Ocular Imaging. *Opt Lett.* 2010; 35:270–272. [PubMed: 20125691]
6. Wang X, Xie X, Ku G, Wang LV, Stoica G. Noninvasive Imaging of Hemoglobin Concentration and Oxygenation in the Rat Brain Using High-Resolution Photoacoustic Tomography. *J Biomed Opt.* 2006; 11:024015. [PubMed: 16674205]
7. Oh JT, Li ML, Zhang HF, Maslov K, Stoica G, Wang LV. Three-Dimensional Imaging of Skin Melanoma in Vivo by Dual-Wavelength Photoacoustic Microscopy. *J Biomed Opt.* 2006; 11:034032.
8. de la Zerda A, Zavaleta C, Keren S, Vaithilingam S, Bodapati S, Liu Z, Levi J, Smith BR, Ma TJ, Oralkan O, et al. Carbon Nanotubes As Photoacoustic Molecular Imaging Agents in Living Mice. *Nature Nanotechnology.* 2008; 3:557–562.
9. Kircher MF, de la Zerda A, Jokerst JV, Zavaleta CL, Kempen PJ, Mittra E, Pitter K, Huang R, Campos C, Habte F, et al. A Brain Tumor Molecular Imaging Strategy Using a New Triple-Modality Mri-Photoacoustic-Raman Nanoparticle. *Nature Medicine.* 2012; 18:829–834.
10. Mallidi S, Larson T, Tam J, Joshi PP, Karpouk A, Sokolov K, Emelianov S. Multiwavelength Photoacoustic Imaging and Plasmon Resonance Coupling of Gold Nanoparticles for Selective Detection of Cancer. *Nano Lett.* 2009; 9:2825–2831. [PubMed: 19572747]

11. Kim JW, Galanzha EI, Shashkov EV, Moon HM, Zharov VP. Golden Carbon Nanotubes As Multimodal Photoacoustic and Photothermal High-Contrast Molecular Agents. *Nat Nanotechnol.* 2009; 4:688–694. [PubMed: 19809462]
12. Eghtedari M, Oraevsky A, Copland JA, Kotov NA, Conjusteau A, Motamedi M. High Sensitivity of in Vivo Detection of Gold Nanorods Using a Laser Optoacoustic Imaging System. *Nano Letters.* 2007; 7:1914–1918. [PubMed: 17570730]
13. Yang X, Skrabalak SE, Li ZY, Xia Y, Wang LV. Photoacoustic Tomography of a Rat Cerebral Cortex in Vivo with Au Nanocages As an Optical Contrast Agent. *Nano Lett.* 2007; 7:3798–3802. [PubMed: 18020475]
14. Agarwal A, Huang SW, O'Donnell M, Day KC, Day M, Kotov N, Ashkenazi S. Targeted Gold Nanorod Contrast Agent for Prostate Cancer Detection by Photoacoustic Imaging. *Journal of Applied Physics.* 2007; 102:064701–064704.
15. Kim G, Huang SW, Day KC, O'Donnell M, Agayan RR, Day MA, Kopelman R, Ashkenazi S. Indocyanine-Green-Embedded Pebbles As a Contrast Agent for Photoacoustic Imaging. *J Biomed Opt.* 2007; 12:044020. [PubMed: 17867824]
16. Zhang Q, Iwakuma N, Sharma P, Moudgil BM, Wu C, McNeill J, Jiang H, Grobmyer SR. Gold Nanoparticles As a Contrast Agent for in Vivo Tumor Imaging with Photoacoustic Tomography. *Nanotechnology.* 2009; 20:395102. [PubMed: 19726840]
17. Bouchard LS, Anwar MS, Liu GL, Hann B, Xie ZH, Gray JW, Wang X, Pines A, Chen FF. Picomolar Sensitivity Mri and Photoacoustic Imaging of Cobalt Nanoparticles. *Proceedings of the National Academy of Sciences of the United States of America.* 2009; 106:4085–4089. [PubMed: 19251659]
18. Levi J, Kothapalli SR, Ma TJ, Hartman K, Khuri-Yakub BT, Gambhir SS. Design, Synthesis, and Imaging of an Activatable Photoacoustic Probe. *J Am Chem Soc.* 2010; 132:11264–11269. [PubMed: 20698693]
19. de la Zerda A, Liu Z, Bodapati S, Teed R, Vaithilingam S, Khuri-Yakub BT, Chen X, Dai H, Gambhir SS. Ultrahigh Sensitivity Carbon Nanotube Agents for Photoacoustic Molecular Imaging in Living Mice. *Nano Letters.* 2010; 10:2168–2172. [PubMed: 20499887]
20. Razansky D, Distel M, Vinegoni C, Ma R, Perrimon N, Koster RW, Ntziachristos V. Multispectral Opto-Acoustic Tomography of Deep-Seated Fluorescent Proteins in Vivo. *Nat Photon.* 2009; 3:412–417.
21. Ntziachristos V, Razansky D. Molecular Imaging by Means of Multispectral Optoacoustic Tomography (Msot). *Chem Rev.* 2010; 110:2783–2794. [PubMed: 20387910]
22. Liu Z, Cai W, He L, Nakayama N, Chen K, Sun X, Chen X, Dai H. In Vivo Biodistribution and Highly Efficient Tumour Targeting of Carbon Nanotubes in Mice. *Nat Nanotechnol.* 2007; 2:47–52. [PubMed: 18654207]
23. de la Zerda A, Kim J-W, Galanzha EI, Gambhir SS, Zharov VP. Advanced Contrast Nanoagents for Photoacoustic Molecular Imaging, Cytometry, Blood Test and Photothermal Theranostics. *Contrast Media & Molecular Imaging.* 2011; 6:346–369. [PubMed: 22025336]
24. Schipper ML, Nakayama-Ratchford N, Davis CR, Kam NWS, Chu P, Liu Z, Sun X, Dai H, Gambhir SS. A Pilot Toxicology Study of Single-Walled Carbon Nanotubes in a Small Sample of Mice. *Nat Nano.* 2008; 3:216–221.
25. Liu Z, Davis C, Cai W, He L, Chen X, Dai H. Circulation and Long-Term Fate of Functionalized, Biocompatible Single-Walled Carbon Nanotubes in Mice Probed by Raman Spectroscopy. *Proceedings of the National Academy of Sciences of the United States of America.* 2008; 105:1410–1415. [PubMed: 18230737]
26. Liu Z, Tabakman S, Welsher K, Dai H. Carbon Nanotubes in Biology and Medicine: In Vitro and in Vivo Detection, Imaging and Drug Delivery. *Nano Research.* 2009; 2:85–120. [PubMed: 20174481]
27. Vaithilingam, S.; Ma, T-J.; Furukawa, Y.; Zerda, Adl; Oralkan, O.; Kamaya, A.; Keren, S.; Gambhir, SS., Jr; RB, J.; Khuri-Yakub, BT. A Co-Axial Scanning Acoustic and Photoacoustic Microscope, *Ultrasonics Symposium, 2007. IEEE; 2007.* p. 2413-2416.
28. American National Standards Institute, American national standard for the safe use of lasers, ANSI Standard Z136.1-2000. New York: ANSI, Inc.; 2000.

29. Loening AM, Gambhir SS. Amide: A Free Software Tool for Multimodality Medical Image Analysis. *Mol. Imaging*. 2003; 2:131–137. [PubMed: 14649056]

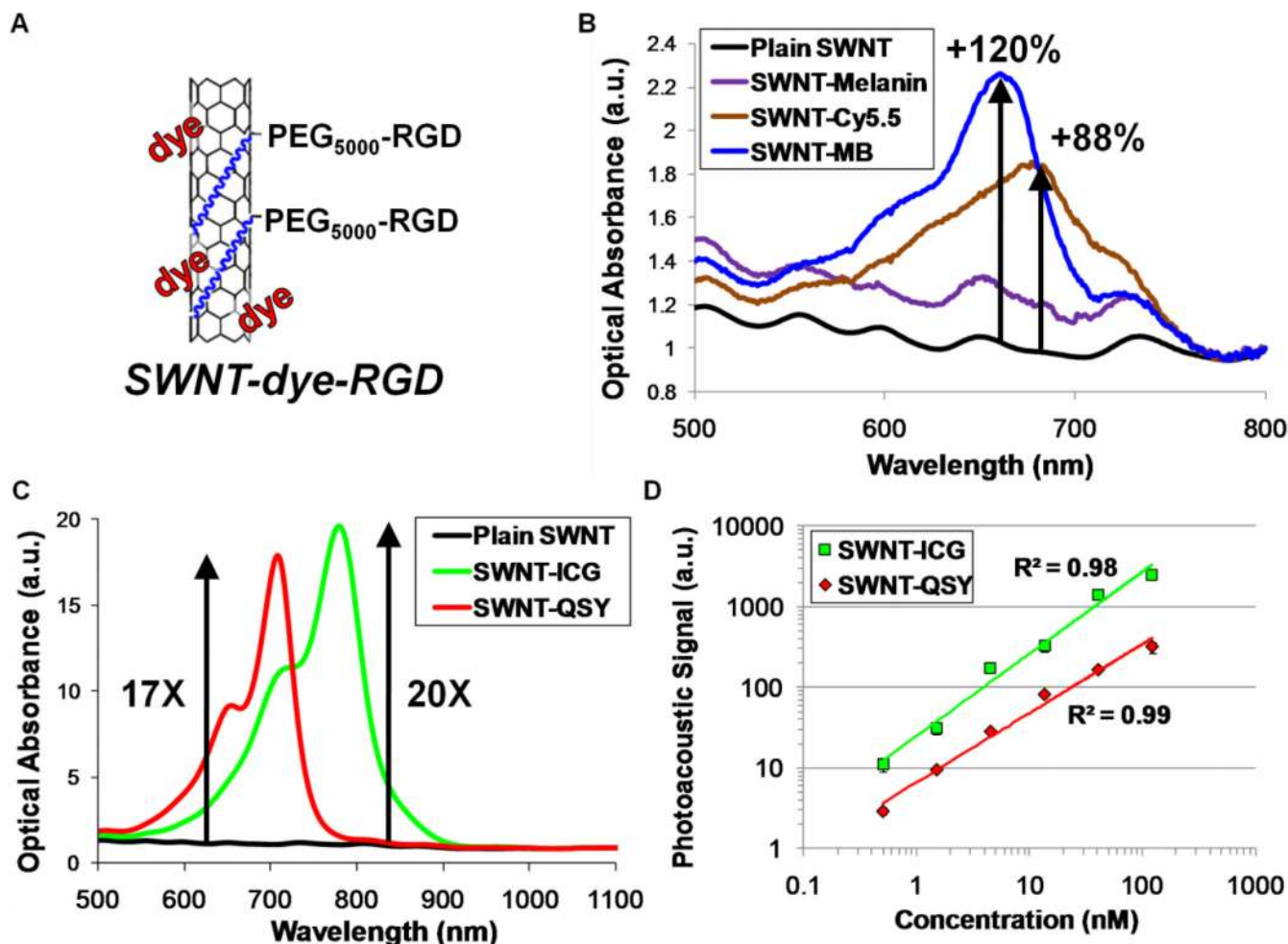


Figure 1. Characterization of the dye-enhanced SWNT

(A) Illustration of a SWNT-dye-RGD particle. The dye (red) is attached to the SWNT surface through non-covalent pi-pi stacking bonds. Phospholipid-polyethylene glycol-5000 (blue) is conjugated to the targeting peptide (RGD) in one end and to the SWNT surface on the other end. (B, C) Optical spectra of (B) plain SWNT (black), SWNT-Melanin (purple), SWNT-Cy5.5 (brown), SWNT-Methylene Blue (blue), (C) SWNT-QSY (red) and SWNT-ICG (green). The QSY and ICG dye-enhanced SWNTs particles showed 17 and 20-times higher optical absorption than plain SWNT at their peak absorption wavelengths, 710 and 780 nm respectively. (D) The photoacoustic signal produced by SWNT-QSY and SWNT-ICG was observed to be linearly dependent on the particles' concentration ($R^2 = 0.99$ and 0.98 respectively).

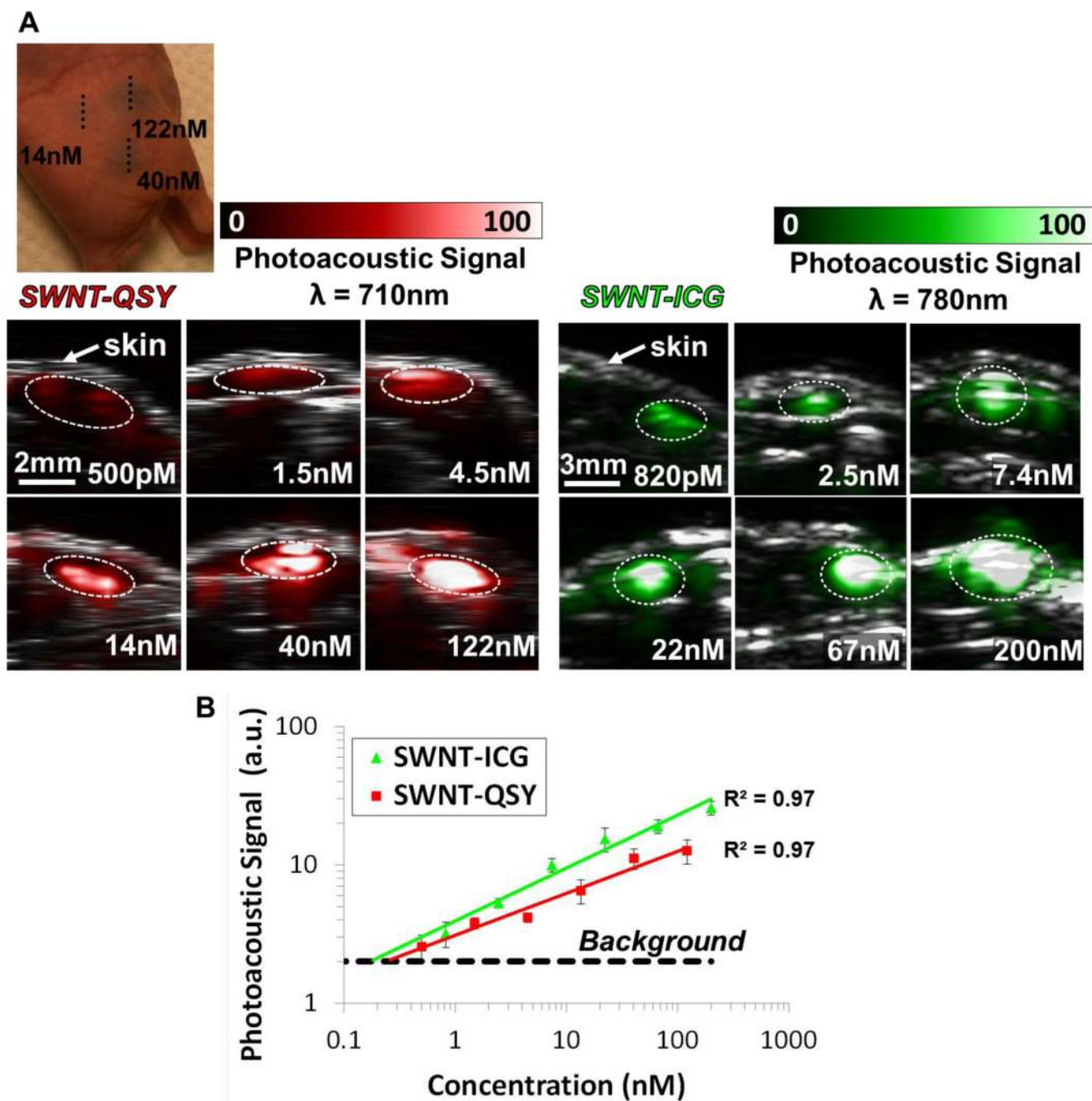


Figure 2. Photoacoustic detection of SWNT-dye particles in living mice

(A) Mice were injected subcutaneously with SWNT-QSY at concentrations between 0.5–122 nM. The images represent ultrasound (gray) and photoacoustic images acquired at $\lambda = 710$ nm (red) as vertical slices through the subcutaneous injections (dotted black line on the mouse picture). Photoacoustic images of mice injected with SWNT-ICG and acquired at $\lambda = 780$ nm (green) are presented for comparison and taken with permission from¹⁹. The skin and inclusion region are visualized in the ultrasound images, while the photoacoustic images visualize the nanoparticles contrast. The white dotted lines on the images illustrate the approximate edges of each inclusion. (B) The photoacoustic signal from each inclusion was

calculated using 3D regions of interest and the 'background' represents the endogenous signal measured from tissues. The error bars represent standard error ($n = 3$ mice). Linear regression ($R^2 = 0.97$ for both particles) of the photoacoustic signal curves estimated that a concentration of 450 pM of SWNT-QSY or 170 pM of SWNT-ICG produces the equivalent background signal of tissues.

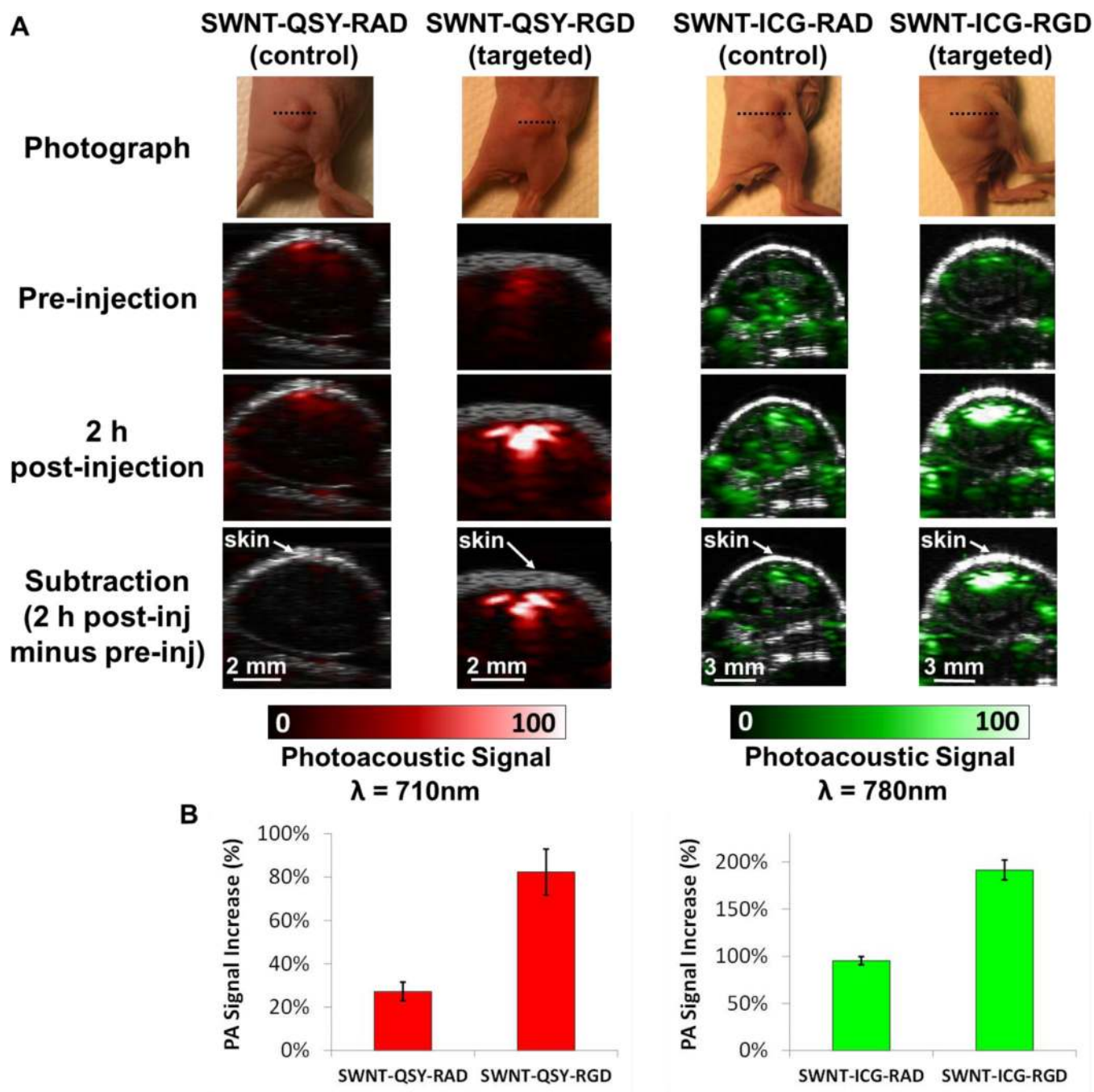


Figure 3. SWNT-dye tumor targeting in living mice

(A) Ultrasound (gray) and photoacoustic (red for $\lambda = 710\text{ nm}$ and green for $\lambda = 780\text{ nm}$) images of a vertical slice through the tumors (dotted black line). The ultrasound images show the skin and the tumor boundaries. Subtraction photoacoustic images were calculated as 2 h post-injection minus pre-injection images. As can be seen in the subtraction images, SWNT-QSY-RGD as well as SWNT-ICG-RGD accumulated in significantly higher amounts in the tumor as compared to their respective control versions. SWNT-ICG images (green) are presented for comparison and are taken with permission from¹⁹. (B) Quantitative region of interest analysis showed that SWNT-QSY-RGD creates a 3-fold higher

photoacoustic signal increase in the tumor than the control SWNT-QSY-RAD particle ($p < 0.01$). SWNT-ICG-RGD provides over 100% higher photoacoustic signal increase than the control SWNT-ICG-RAD ($p < 0.01$). The error bars represent standard error ($n = 3$ mice)

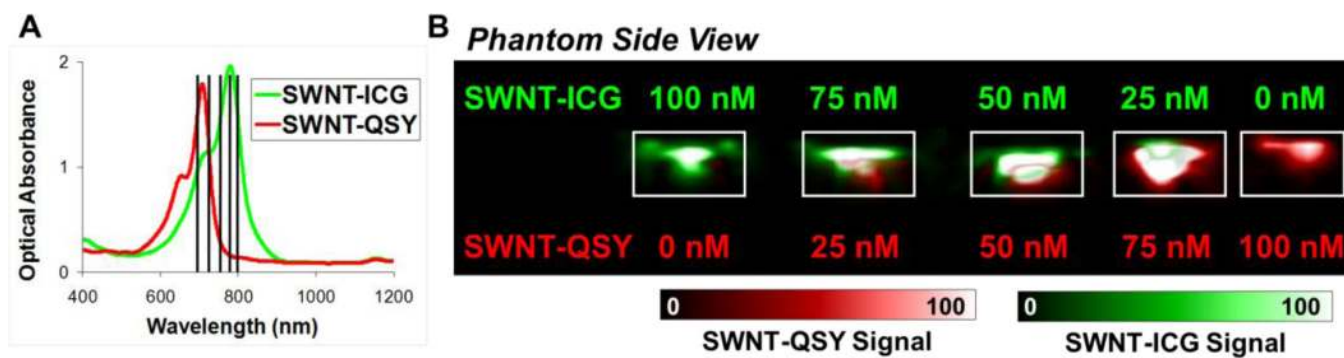


Figure 4. Multiplexing of SWNT-QSY and SWNT-ICG *in vitro*

(A) An agarose phantom containing SWNT-ICG and SWNT-QSY at different mixture concentrations (pure SWNT-ICG, 1:3, 1:1, 3:1 and pure SWNT-QSY) was scanned using the photoacoustic instrument at 5 different wavelengths (700, 730, 760, 780, 800 nm). (B) Despite their overlapping spectra, the photoacoustic signals from SWNT-QSY (red) and SWNT-ICG (green) were unmixed well by the least squares algorithm.

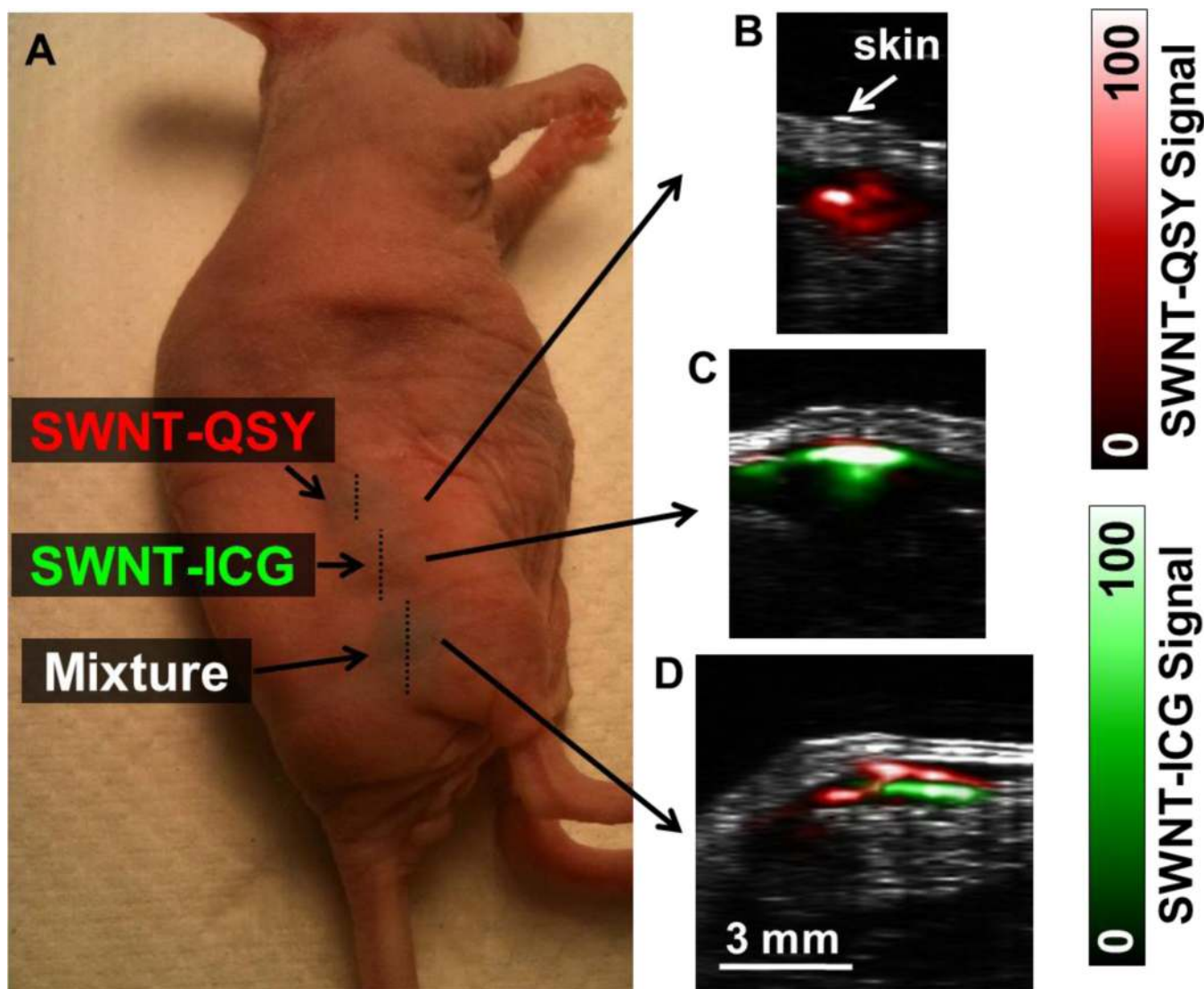


Figure 5. Multiplexing of SWNT-QSY and SWNT-ICG in living mice

(A) A mouse was injected with 30 μ l of 50 nM SWNT-QSY (upper inclusion), 30 μ l of 50 nM SWNT-ICG (middle inclusion) and 30 μ l of an equal mixture of 50 nM of SWNT-QSY and SWNT-ICG (lower inclusion). (B) The unmixed photoacoustic vertical slice through the upper inclusion, showing only SWNT-QSY signal (red). (C) The unmixed photoacoustic slice through the middle inclusion showed mostly SWNT-ICG signal (green). (D) The unmixed photoacoustic slice through the lower inclusion, showing both SWNT-QSY and SWNT-ICG signals spread throughout the inclusion area. Image reconstruction artifacts as well as inhomogeneous light penetration into the tissue are likely the cause for the separation of the green and red signals in the image.